

Genetically inspired in vitro reconstitution of *Saccharomyces cerevisiae* actin cables from seven purified proteins

Luther W. Pollard, Mikael V. Garabedian, Salvatore L. Alioto, Shashank Shekhar, and Bruce L. Goode*

Department of Biology, Brandeis University, Waltham, MA 02454

ABSTRACT A major goal of synthetic biology is to define the minimal cellular machinery required to assemble a biological structure in its simplest form. Here, we focused on *Saccharomyces cerevisiae* actin cables, which provide polarized tracks for intracellular transport and maintain defined lengths while continuously undergoing rapid assembly and turnover. Guided by the genetic requirements for proper cable assembly and dynamics, we show that seven evolutionarily conserved *S. cerevisiae* proteins (actin, formin, profilin, tropomyosin, capping protein, cofilin, and AIP1) are sufficient to reconstitute the formation of cables that undergo polarized turnover and maintain steady-state lengths similar to actin cables in vivo. Further, the removal of individual proteins from this simple in vitro reconstitution system leads to cable defects that closely approximate in vivo cable phenotypes caused by disrupting the corresponding genes. Thus, a limited set of molecular components is capable of self-organizing into dynamic, micron-scale actin structures with features similar to cables in living cells.

Monitoring Editor

Fred Chang
University of California,
San Francisco

Received: Oct 18, 2019

Revised: Dec 16, 2019

Accepted: Jan 3, 2020

INTRODUCTION

Self-organization is a central theme in biological systems (Misteli, 2001; Karsenti, 2008; Wedlich-Soldner and Betz, 2018). However, we presently have a limited understanding of how the dimensions of large, micron-scale structures in cells are established and maintained by their nanometer-scale components, particularly while their subunits continuously disassociate and recycle (Levy and Heald, 2012; Marshall, 2016).

The actin cables of budding yeast (*Saccharomyces cerevisiae*) are a prime example of this phenomenon, exhibiting rapid assembly at one end and disassembly at the other (at ~ 200 subunits s^{-1} [Yang and Pon, 2002; Yu *et al.*, 2011]), while maintaining lengths that match the dimensions of the compartment in which they are formed

($5.3 \pm 2.5 \mu m$; Eskin *et al.*, 2016). Yeast cables are assembled at the bud tip and bud neck by the formins Bni1 and Bnr1, respectively (Figure 1, A and B) (Moseley and Goode, 2006). Cables assembled by Bni1 appear to be released from the bud tip, with Bni1 remaining attached to their ends, and move in a retrograde manner toward the mother cell (Buttery *et al.*, 2007). Similar observations have been made in *Schizosaccharomyces pombe*, where the formin For3 is released with cables from cell tips (Martin and Chang, 2006). In contrast to Bni1, the formin Bnr1 stays anchored at the bud neck via interactions with septins and septin-associated proteins (Buttery *et al.*, 2007, 2012; Gao *et al.*, 2010), and the cables it polymerizes grow while they are attached to Bnr1 at the neck; cables extend toward the rear of the mother cell while being turned over by disassembly factors (Okada *et al.*, 2006; Yu *et al.*, 2011; Graziano *et al.*, 2014; Eskin *et al.*, 2016; Garabedian *et al.*, 2018). Overall, the current view of cable networks is that they are continuously assembled by formins at the bud tip and neck, extend rearward toward the back of the mother cell at a rate of ~ 0.3 – $1.0 \mu m/s$, contouring the cell cortex, and are trimmed and depolymerized by cofilin and other factors (Goode *et al.*, 2015).

The precise architecture of *S. cerevisiae* actin cables has yet to be determined. Cables are often depicted in models as parallel bundles, consisting of shorter, overlapping filaments cross-linked to each other with their barbed ends oriented toward the bud tip (Moseley and Goode, 2006). This view is based primarily on two

This article was published online ahead of print in MBoC in Press (<http://www.molbiolcell.org/cgi/doi/10.1091/mbc.E19-10-0576>) on January 8, 2020.

*Address correspondence to: Bruce L. Goode (goode@brandeis.edu).

Abbreviations used: BSA, bovine serum albumin; CCA, Cof1, Cnm1, and Aip1; DTT, dithiothreitol; EGTA, ethylene-bis(oxyethylenenitrilo)tetraacetic acid; GST, glutathione S-transferase; OG, Oregon Green; PBS, phosphate-buffered saline; PEG, polyethylene glycol; RMA, rabbit muscle actin; SIM, superresolution structured illumination microscopy; WT, wild type.

© 2020 Pollard *et al.* This article is distributed by The American Society for Cell Biology under license from the author(s). Two months after publication it is available to the public under an Attribution–Noncommercial–Share Alike 3.0 Unported Creative Commons License (<http://creativecommons.org/licenses/by-nc-sa/3.0>).

“ASCB®,” “The American Society for Cell Biology®,” and “Molecular Biology of the Cell®” are registered trademarks of The American Society for Cell Biology.

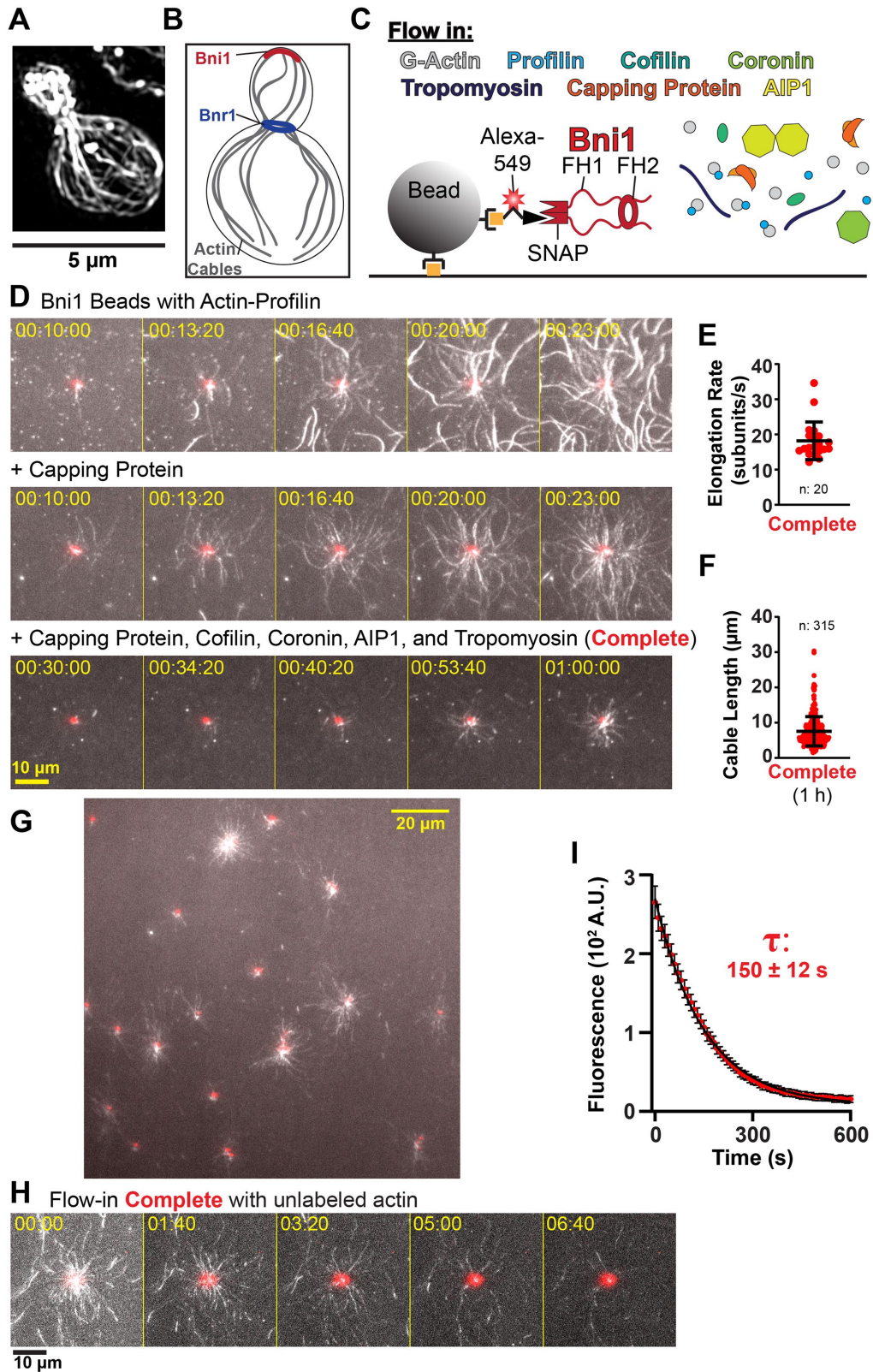


FIGURE 1: In vitro reconstitution of dynamic actin cables from purified *S. cerevisiae* proteins. (A) SIM image of a fixed, Alexa⁴⁸⁸-phalloidin-stained WT yeast cell. (B) Cartoon highlighting the locations of *S. cerevisiae* formins Bni1 and Bnr1 during polarized cell growth, from which they polymerize actin cables. (C) Components of the in vitro actin cable reconstitution system. Avidin-coated beads (gray) bind to biotin (yellow squares) on the viewing surface and on biotin-Alexa⁵⁴⁹-SNAP-Bni1 molecules. Reactions contain (as indicated): 1 μM actin (15% OG-labeled), 1 μM profilin (Pfy1), 2 μM tropomyosin (Tpm1), 30 nM capping protein (Cap1/2), 200 nM cofilin (Cof1), 20 nM coronin (Crn1), and 20 nM AIP1 (Aip1). (D) Time points from TIRF imaging of cable assembly (also see Supplemental Movie S1). Actin filaments in

observations: 1) cables are decorated by proteins that bundle actin filaments in vitro, for example, Sac6/fimbrin and Abp140 (Drubin *et al.*, 1988; Asakura *et al.*, 1998); however, these proteins may also be capable of decorating single (nonbundled) filaments; 2) a classic EM study in *S. pombe* found linear bundles of actin in the cytosol, consisting of overlapping shorter filaments (Kamasaki *et al.*, 2005). It is important to note, however, that fluorescence imaging studies have shown that cables in the bud are often much less intense than cables in the mother; this raises the possibility that some cables are only a single filament thick while others are bundles.

One of the first steps in understanding the assembly of any complex cellular structure is to define its parts. Over the years, genetic studies have established that proper cable formation requires formins, profilin (Pfy1), tropomyosin (Tpm1), and capping protein (Cap1/2) (Haarer *et al.*, 1990; Adams *et al.*, 1993; Pruyne *et al.*, 1998; Evangelista *et al.*, 2002; Sagot *et al.*, 2002), and that normal cable turnover and/or morphology further requires cofilin (Cof1), coronin (Crn1), and actin-interacting protein/AIP1/WDR1 (Aip1) (Iida *et al.*, 1993; Moon *et al.*, 1993; Rodal *et al.*, 1999; Okada *et al.*, 2006; Gandhi *et al.*, 2009). However, it has been unclear whether these molecular parts are sufficient to assemble an actin cable in its simplest form (with a size and turnover properties similar to cables in vivo and dependent on distinct contributions made by the individual components).

One powerful approach for elucidating the design principles of cellular structures is through in vitro reconstitution (Ganzinger and Schwille, 2019). A seminal example was the in vitro reconstitution of Arp2/3-based branched actin networks that propel *Listeria*, which validated many of the core principles of actin network dynamics and helped define the molecular basis of motility (Loisel *et al.*, 1999). More recently, a number of studies have made important advances in reconstituting linear, formin-generated actin structures. In doing so, these studies have provided new insights into formin mechanism (Romero *et al.*, 2007), revealed how stochastic severing and disassembly by cofilin can balance formin-mediated polymerization (Michelot *et al.*, 2007), and demonstrated that formins and Arp2/3 complex compete for a limited pool of actin monomers and differentially collaborate with other actin regulatory proteins to build distinct actin networks (Suarez *et al.*, 2015; Antkowiak *et al.*, 2019). Moreover, top-down studies in yeast cell extracts have reconstituted contractile acto-myosin rings (Mishra *et al.*, 2013) and linear cable-like structures (Miao *et al.*, 2013, 2016).

Here, we build on these studies and take a genetically inspired biochemical approach to defining, from the bottom-up, a minimal set of purified proteins that is sufficient to assemble actin cables. We show that the reconstituted cables undergo polarized assembly and turnover and reach steady-state lengths similar to cables in vivo. Further, the removal of specific components leads to cable defects in vitro which resemble cable phenotypes caused by mutating the

same genes in vivo. Our results shed new light on the roles that tropomyosin and several actin disassembly factors play in cable formation and more broadly demonstrate that a minimal set of proteins, defined by genetic requirements for cable formation in vivo, is sufficient to self-organize into cables in vitro.

RESULTS AND DISCUSSION

On the basis of the genetic studies discussed above, we purified eight *S. cerevisiae* proteins and attempted to reconstitute the assembly of actin cables that 1) are polymerized at their barbed ends by formins, 2) turn over in a polarized manner via disassembly factors, and 3) grow to reach steady-state lengths similar to cable networks in vivo. To accomplish this, we attached the constitutively active C-terminal half (FH1-FH2-C) of the formin Bni1 to beads and anchored the beads to the glass coverslip. We used Bni1 rather than Bnr1, because it plays a more prominent role in cable assembly throughout the cell cycle and in mating cells, and its in vitro activities are more well defined. We then flowed in G-actin and other protein components and imaged actin assembly by TIRF microscopy (Figure 1C). Specific concentrations of proteins used were defined experimentally by titration, guided by previous in vitro studies on mammalian counterparts (Jansen *et al.*, 2015; Shekhar and Carlier, 2017; Jansen and Goode, 2019), and by our goal of producing clearly visible cable networks with a limited background of surrounding filaments (by inclusion of Pfy1, Cap1/2, and Cof1), and that undergo turnover (by inclusion of Cof1, Aip1, and Crn1).

After flowing in G-actin and profilin alone, cables grew into dense networks (Figure 1D) with many free filaments surrounding the beads, presumably arising from spontaneous nucleation. The further addition of Cap1/2 reduced free filaments in the background (Figure 1D), which enabled us to measure cable elongation rates (17.5 ± 3.5 subunits s^{-1} at $1 \mu M$ actin-profilin; \pm SD, $n = 15$ cables; Table 1). This rate was similar to reported Bni1 polymerization rates (Kovar *et al.*, 2006). However, in these reactions, cable networks continued to elongate until they grew into each other, indicating that their lengths were not regulated.

Adding Tpm1 and three disassembly promoting factors, Cof1, Crn1, and Aip1 (CCA), prevented network overgrowth (Figure 1D) and produced cables that elongated at 18.2 ± 5.4 subunits s^{-1} (\pm SD, $n = 20$ cables; Figure 1E) and maintained steady-state lengths ($7.6 \pm 4.1 \mu m$; \pm SD, $n = 315$ cables; Figure 1, F and G) similar to cables in vivo ($5.3 \pm 2.5 \mu m$; Eskin *et al.*, 2016). Under these conditions, all visible F-actin assembly was dependent on the Bni1-coated beads (Supplemental Figure S1), and cables reached a state where assembly and stabilization (by Bni1, profilin, and Tpm1) were balanced by disassembly (mediated by CCA). We also observed that cable disassembly occurred by stochastic severing and shortening of cables (Supplemental Movie S1), with release of fragments, consistent with the reported activities of CCA (Rodal *et al.*, 1999; Briehner *et al.*, 2006; Jansen *et al.*, 2015; Mikati *et al.*, 2015). Altogether, these

grayscale and formin-coated beads in red. Time stamps in hours (h): minutes (min): seconds (s). (E) Cable elongation rates for Complete mixtures (all eight proteins). Data from two experiments ($n = 20$ cables). Error bars, SD. (F) Cable lengths in Complete mixtures at steady state (1 h after assembly was initiated). Data from five experiments ($n = 315$ cables). Error bars, SD. (G) A TIRF field showing discrete cable networks assembled around beads with the Complete mixture at steady state (1 h). Variability in levels of active formins attached to the beads leads to variability in cable network density surrounding beads. (H) Demonstration of polarized turnover in cable networks (Supplemental Movie S2). Reactions as in D containing the Complete mixture were allowed to reach steady state, and then an identical reaction mixture with unlabeled actin was flowed in at time zero. Time stamps, minutes (min): seconds (s). (I) Quantification from reactions as in H of the decay in actin fluorescence surrounding the beads (within $10 \mu m$) over time. Data averaged from two experiments ($n = 46$ beads). Data were fitted to a single exponential, with the lifetime (τ) shown. Error bars, SEM.

In vitro				In vivo			
Cable elongation rates				Strain	Fluor. (% WT)	Cells	P value
Condition	Rate (subunits s ⁻¹)	Cables (n)	Trials (N)	Untreated phalloidin-stained cells in SIM			
1 μM actin, 1 μM Pfy1, 2 μM Tpm1, 30 nM Cap1/2, 200–20–20 nM CCA				Total cable fluorescence in the mother compartment			
Complete	18.2 ± 5.4	20	2	WT	100 ± 32	15	
-CCA -Tpm1	17.5 ± 3.5	15	2	tpm1Δ	20 ± 9	10	<0.0001
-Pfy1	3.0 ± 1.6	6	2	pfy1Δ	6 ± 4	10	<0.0001
Cable length				CK666-treated phalloidin-stained cells in confocal			
1 μM actin, 1 μM Pfy1, 2 μM Tpm1, 40 nM Cap1/2, 300 nM Cof1, 20 nM Crn1, 20 nM Aip1				Fluorescence of cables per cell area			
Condition	Length (μm)	Cables (n)	Trials (N)	WT <td>100 ± 33</td> <td>100</td> <td></td>	100 ± 33	100	
Complete	7.6 ± 4.1	315	5	tpm1Δ	75 ± 33	100	0.0008
-Tpm1	Approx. zero		3	cof1-22	285 ± 66	50	<0.0001
-Pfy1	4.3 ± 2.8	50	3	aip1Δ	126 ± 32	100	0.0012
-Aip1	10.2 ± 3.8	100	3	crn1Δ	114 ± 33	50	>0.99
-Crn1	8.2 ± 4.7	200	3	Fluorescence of cables per mother area			
-Tpm1 -Aip1	5.5 ± 2.2	100	3	WT	100 ± 29	30	
Cables per bead				pfy1Δ	76 ± 19	30	0.023
1 μM actin, 1 μM Pfy1, 2 μM Tpm1, 40 nM Cap1/2, 300 nM Cof1, 20 nM Crn1, 20 nM Aip1				cap2Δ	148 ± 48	30	0.0012
Condition	Cables	Beads (n)	Trials (N)				
Complete	6.4 ± 2.9	80	3				
-Tpm1	0.2 ± 1.0	80	3				
-Pfy1	0.9 ± 1.1	80	3				
Actin fluorescence surrounding beads							
1 μM actin, 1 μM Pfy1, 2 μM Tpm1, 40 nM Cap1/2, 300 nM Cof1, 20 nM Crn1, 20 nM Aip1							
Condition	Fluor. (% complete)	Beads (n)	Trials (N)				
Complete	100 ± 9	86	3				
-Cap1/2	163 ± 63	77	3				
-Cof1	133 ± 63	64	3				
-Aip1	133 ± 24	53	3				
-Crn1	95 ± 14	86	3				
-Tpm1 -Aip1	101 ± 12	70	3				

P values are derived from Kruskal-Wallis tests.

TABLE 1: Cable statistics.

results show that eight purified proteins are sufficient to reconstitute cables that meet our starting criteria (above).

To measure the rate of turnover, we assembled cable networks with the Complete mixture (including labeled actin) and then flowed in an identical mixture containing unlabeled actin (Figure 1H and Supplemental Movie S2). After flow-in, cable fluorescence decayed over time, yielding a characteristic lifetime of 150 ± 12 s (\pm SD, $n = 46$ beads; Figure 1I). From the average cable length of $7.6 \mu\text{m}$, we calculated the turnover rate: 18.7 ± 1.5 subunits s^{-1} . This value closely matches the elongation rate (18.2 ± 5.4 subunits s^{-1}) and confirms the steady-state balance between cable assembly and disassembly.

We next examined the effects of omitting individual components from our in vitro mixtures in order to better understand their functions (Figure 2). As expected, removing profilin, which is a key cofactor of formins in actin assembly, resulted in fewer and shorter cables (Figure 2B; Table 1). In contrast, removal of CCA greatly increased cable density, indicating that these factors limit cable growth. Under these conditions, the cable density was too high to count cables accurately, so we instead compared levels of OG-actin fluorescence around the beads (Figure 2C). Removal of coronin led to no obvious defects in cable levels, which is consistent with *crn1* Δ not altering cable staining in vivo (Goode et al., 1999). This demonstrates that seven proteins are sufficient to reconstitute dynamic cables in vitro. Removal of tropomyosin, which decorates the sides of actin filaments and protects them from CCA (Jansen and Goode, 2019), nearly abolished cable assembly. In contrast, another recent study concluded that tropomyosin was not necessary for robust cable assembly in vitro, even though it is required for cable assembly in vivo (Antkowiak et al., 2019). We suggest that this discrepancy arises because of the absence of AIP1 in their in vitro system. We have previously shown that *aip1* Δ suppresses loss of cables in *tpm1* Δ mutants in vivo (Okada et al., 2006), and indeed, removing Aip1 and tropomyosin together from our in vitro mixtures restores cables (Figure 2, A and C). Thus, our purified system reconstitutes the in vivo antagonism between tropomyosin and Aip1.

To more carefully examine how well our in vitro system mimics in vivo requirements for cable assembly, we compared actin cable organization in wild-type (WT) and mutant yeast strains. To date, the effects of different mutants on cable levels and appearance have come from a variety of genetic studies performed in different labs, often using different strain backgrounds and imaging approaches. Therefore, we generated one isogenic set of strains to analyze and directly compared them for cable organization by superresolution structured illumination microscopy (SIM) (Figure 3A) and cable density by confocal microscopy (Figure 3, B–D). Further, we examined cable organization in the same strains after treatment with CK666 (an Arp2/3 complex inhibitor) to remove actin patches (Suarez and Kovar, 2016). There are both merits and caveats to analyzing mutant effects on cable networks after CK666 treatment. The major caveat is that loss of actin patches shifts the entire cellular pool of actin to cables, leading to WT cells with increased cable density (Burke et al., 2014; Antkowiak et al., 2019). However, a merit of this approach is that it eliminates any indirect effects on cables stemming from changes in actin patches, for example, in the absence of CK666, *cap2* Δ results in enlarged actin patches, which ties up more of the actin and indirectly leads to diminished cables (Antkowiak et al., 2019). Another merit of using CK666 is that it eliminates the otherwise bright-staining actin patches, so that one can more accurately measure and compare cable levels between mutant and WT cells (understanding that there is an artificially high baseline in WT).

By manually tracing and quantifying cable lengths and intensities in untreated cells (no CK666) imaged by SIM, we found that *tpm1* Δ and *pfy1* Δ caused a severe loss of cables, while other mutants (*cap2* Δ , *cof1*-22, and *aip1* Δ) caused more modest reductions (Table 1; example images in top panels, Figure 3A). These observations agree well with previous studies (Amatruda et al., 1990; Haarer et al., 1990; Pruyne et al., 1998; Goode et al., 1999; Rodal et al., 1999; Ydenberg et al., 2015; Antkowiak et al., 2019). In CK666-treated cells, *tpm1* Δ and *pfy1* Δ each resulted in severely diminished cables, whereas *cap2* Δ , *cof1*-22, and *aip1* Δ each caused an increase in cable density relative to WT cells (bottom panels, Figure 3A). *Crn1* Δ was not significantly different from WT, consistent with our in vitro results showing that Crn1 does not make a substantial contribution to cable reconstitution. Quantification of F-actin density (total fluorescence divided by cell area) in CK666-treated cells (Figure 3B) agreed with these observations, with two notable exceptions: *pfy1* Δ and *cap2* Δ . These mutants each had residual actin patches despite CK666 treatment (Figure 3A), although the reason for patch resistance to CK666 in these mutants is not yet clear. To address this problem, we measured F-actin density specifically in the mother compartment, as many of the patches were in the bud; we observed a decrease in cable density in *pfy1* Δ and an increase in *cap2* Δ compared with WT (Figure 3C). Overall, there was good agreement between our in vitro and in vivo data on the cable defects caused by removing specific components (Figures 2 and 3). In this respect, our in vitro reconstitution system appears to be biomimetic.

The results above suggested that a balance between Tpm1 and CCA activities might govern cable length. To probe this idea further, we compared steady-state cable length in vitro in the presence and absence of Tpm1, at both a standard or a reduced concentration of CCA (Figure 4, A and B). At the standard concentration of CCA (same as used above), cables were undetectable without Tpm1, and long cables were observed with Tpm1 ($7.0 \pm 3.4 \mu\text{m}$; \pm SD, $n = 185$). However, at the reduced concentration of CCA, long cables now formed in the absence of Tpm1 ($7.9 \pm 3.4 \mu\text{m}$; \pm SD, $n = 75$). Further, cable length increased with Tpm1 present ($8.8 \pm 4.0 \mu\text{m}$; \pm SD, $P = <0.0001$, $n = 127$). When CCA concentration was increased further, cables became very short and difficult to visualize, and when CCA concentration was decreased further, cable networks grew into each other. In both cases, this precluded measuring steady-state lengths. Taken together, these data suggest that cable turnover is driven by CCA, and that Tpm1 delays CCA-mediated disassembly to allow cables to reach micron lengths while still turning over. Further, they suggest that proper cable length in this system is supported by a narrow concentration range of CCA.

To better understand the working relationship between Tpm1 and CCA components on cables, we also examined decoration of cables by Cy3-labeled Cof1. In WT cells, Cof1 promotes cable turnover but is not visible on cables; however, in *aip1* Δ cells, Cof1 becomes visible on cables, suggesting that Cof1 may accumulate on actin filaments when cable turnover is impaired (Rodal et al., 1999; Okada et al., 2006). To test whether a similar relationship exists in our in vitro system, we removed Aip1 from the mixture and asked how this affects Cy3-Cof1 decoration of cables (Figure 4C). In Complete mixtures (containing Aip1), Cy3-Cof1 was not visible on cables, similar to what is observed in WT cells. However, in mixtures lacking Aip1, Cy3-Cof1 was now clearly visible on cables, similar to what is observed in *aip1* Δ cells. Similar results were observed in mixtures that excluded Aip1 and Tpm1 together, demonstrating that Cy3-Cof1 decoration (in the absence of Aip1) is not Tpm1-dependent. On the basis of these observations, we propose that

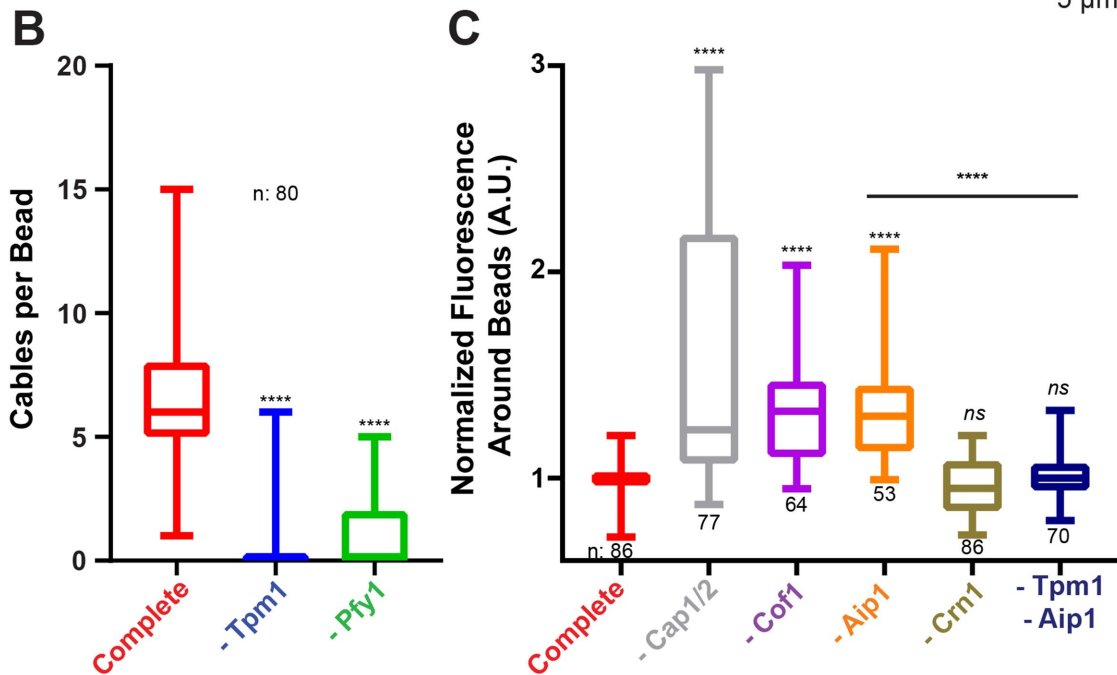
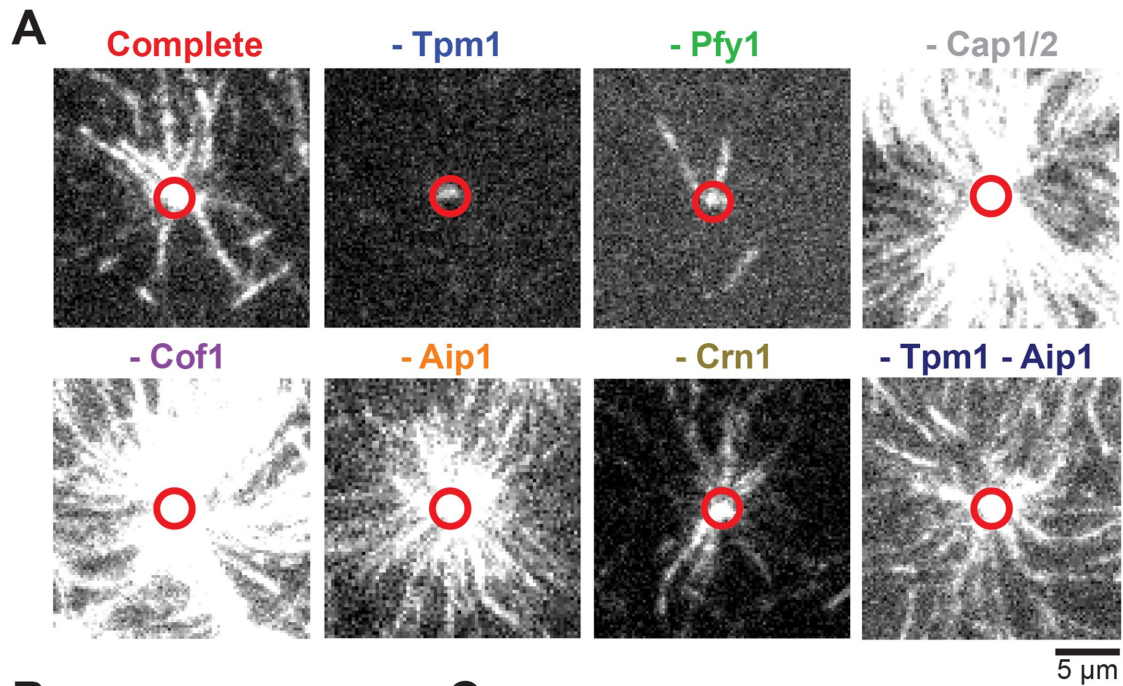


FIGURE 2: Effects on cable assembly in vitro from removing individual components. (A) Representative TIRF micrographs of in vitro reconstituted cable networks at steady state (1 h) in the absence of the indicated component(s). Reactions contain (as indicated): 1 μ M actin (15% OG-labeled), 1 μ M profilin (Pfy1), 2 μ M tropomyosin (Tpm1), 40 nM capping protein (Cap1/2), 300 nM cofilin (Cof1), 20 nM coronin (Crn1), and 20 nM AIP1 (Aip1). Note: these concentrations are slightly different from those in Figure 1, as there was some variability between experiments in the levels of spontaneous actin nucleation, which required minor tuning of the concentrations of Cap1/2 and Cof1. OG-labeled actin cables in grayscale. Alexa⁵⁴⁹-SNAP-Bni1 beads indicated by red open circles. (B) Quantification of cable numbers. Data from three experiments ($n = 80$ beads per condition). (C) Quantification of cable fluorescence levels surrounding the beads in different reactions, normalized to Complete mixture. Note that "-Tpm1" and "-Pfy1" were not included in this analysis because the signal-to-noise ratio was too poor in these reactions. Data were from three experiments ($n =$ total number of beads analyzed per condition, indicated below each box-and-whisker plot). One-way ANOVA significance shown above plots for each condition compared with the Complete mixture (see *Materials and Methods* for asterisk definitions). Additional bars are for indicated pairs.

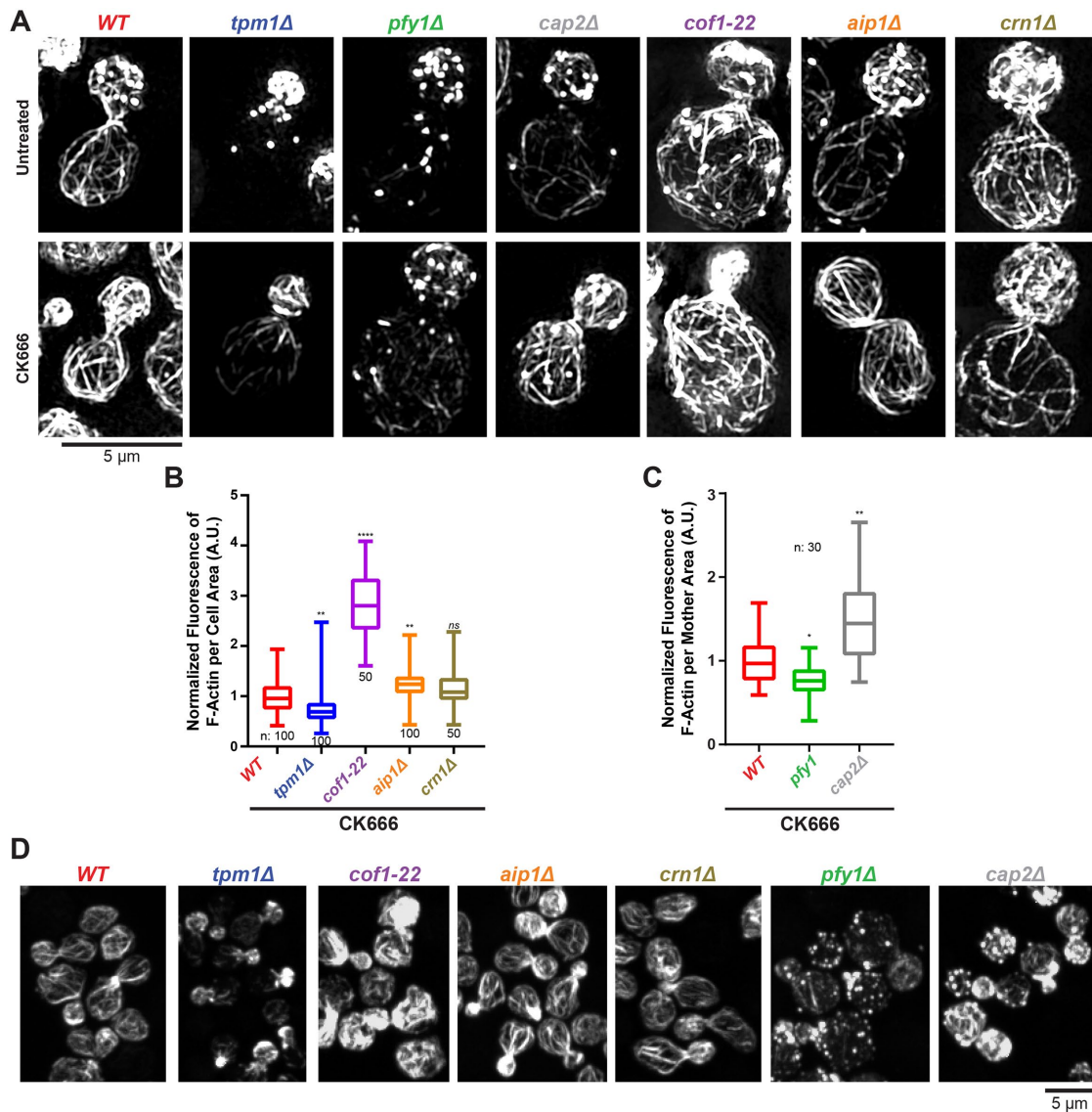


FIGURE 3: Mutant effects on actin cable formation in vivo. (A) Representative SIM images (maximum projection) comparing Alexa⁴⁸⁸-phalloidin-staining of F-actin structures in WT and mutant yeast cells. Bottom panels show cells treated with CK666 to inhibit actin assembly at cortical patches. (B) Quantification in CK666-treated cells of total cellular F-actin density (Alexa⁴⁸⁸-phalloidin fluorescence per unit area) ($n = 50$ – 100 cells per condition). (C) Quantification of F-actin density (Alexa⁴⁸⁸-phalloidin fluorescence per unit area) in the mother compartment of CK666-treated cells ($n = 30$ cells per condition). Box-and-whisker plots show median, range, and upper and lower quartiles. One-way ANOVA significance is shown for each condition compared with WT control (see *Materials and Methods* for asterisk definitions). (D) Representative confocal images of cells stained with Alexa⁴⁸⁸-phalloidin, used for analysis in B and C.

Tpm1 delays the combined disassembly activities of Cof1 and Aip1, enabling cables to reach micron lengths (Figure 4D).

Taken together, these results (along with those in Figure 2) demonstrate that the components of our in vitro reconstitution system contribute to cable formation in a manner that closely resembles their in vivo contributions. Previous cable reconstitution systems have shown that steady-state length and turnover can be achieved in the absence of some of the components we include (AIP1, tropomyosin, and capping protein) (Michelot *et al.*, 2007). However, in developing our reconstitution system, it became clear that capping protein is required to inhibit spontaneous actin assembly away from the formin-coated beads, and that AIP1 is required to produce robust Cof1-dependent disassembly/turnover of cables and to prevent Cy3-Cof1 accumulation on cables. In the combined presence

of Cof1 and AIP1, Tpm1 then becomes essential to grow micron-long cables. Interestingly, the other major actin structure in yeast cells, cortical actin patches, are assembled by a distinct actin nucleator (Arp2/3 complex) and rapidly turned over by Cof1 and AIP1, but are not decorated by tropomyosin. Patches are comparatively small networks, only ~ 0.15 μm long (Kukulski *et al.*, 2012), whereas cables grow to ~ 5 μm in length. This explains why tropomyosin is so crucial for cable but not patch formation.

How then is tropomyosin specifically targeted to cables? Recent studies from the Kovar lab show that tropomyosin and fimbrin directly compete for binding to F-actin, which leads to their sorting to cables and patches, respectively (Skau and Kovar, 2010; Christensen *et al.*, 2017, 2019). Further, our results suggest that tropomyosin decoration allows the assembly of long, linear actin

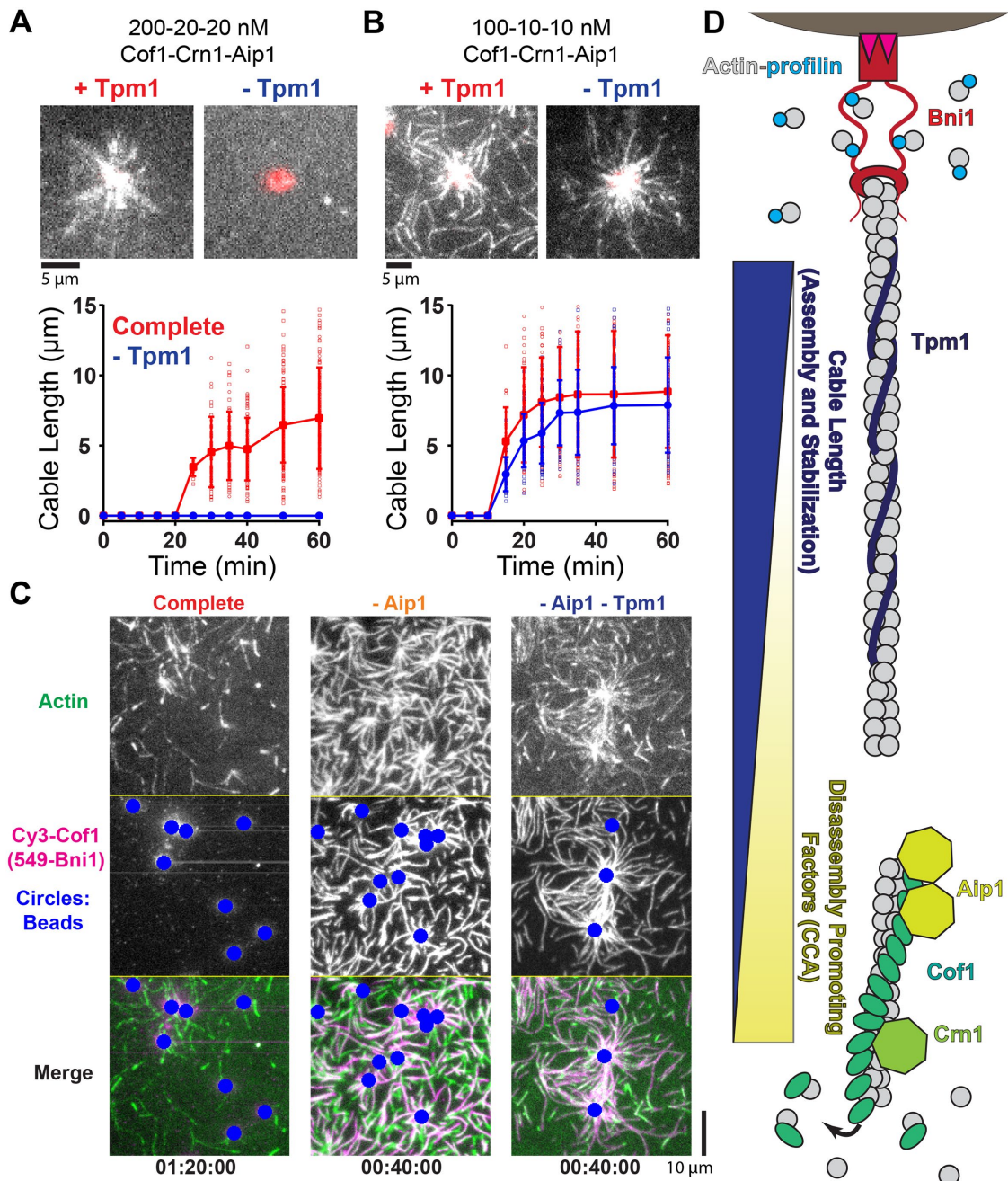


FIGURE 4: Tpm1 increases cable length by antagonizing CCA-mediated actin disassembly. (A, B) Comparison of cable lengths in vitro with (+) and without (-) Tpm1 (2 μ M) in the presence of a higher (A) or a lower (B) concentration of CCA. Concentrations of CCA indicated above panels. All reactions contained: 1 μ M actin (15% OG-labeled), 1 μ M profilin (Pfy1), and 40 nM capping protein (Cap1/2). Top panels show representative TIRF images of cable networks at steady state (1 h), with actin in grayscale and Bni1-beads in red. Plots show mean cable length at different time points in the reaction. Data pooled from two experiments ($n = 6-185$ cables, increasing with time). Error bars, SD. (C) Representative TIRF images showing Cy3-Cof1 (300 nM) decoration of cables assembled in a Complete mixture, or mixtures with specific components removed as indicated. Top and middle rows show OG-actin and Cy3-Cof1, respectively, in grayscale. Blue circles show bead positions. Bottom row shows merged images, with Cy3-Cof1 in magenta and OG-actin in green. Time stamps in hours (h): minutes (min): seconds (s). (D) Working model for how steady-state cable length is tuned through balance of filament stabilization by tropomyosin and turnover by CCA.

structures in a cytosolic environment where robust disassembly by cofilin and AIP1 ensures the rapid turnover of the more dense, branched networks composed of shorter actin filaments. In this manner, elongated linear actin structures such as those generated by formins can be assembled in the same environment that sup-

ports rapid turnover of Arp2/3-generated networks. Altogether, these observations from multiple groups begin to explain the rules for self-organization that allow two actin networks of very different size and filamentous architecture to assemble side-by-side in a shared cytoplasm.

MATERIALS AND METHODS

Plasmids and yeast strains

For expression of tagged 6xHis-SNAP-Bni1^{1228–1953} (FH1-FH2-C-terminus), the plasmid pBG1919 was constructed by restricting the Bni1 coding sequence from pBG564 (Moseley *et al.*, 2006) and ligating it between the *Bam*HI and *Not*I sites of pCG105, a modified pRS426 (*URA3*, 6 × His, *GAL1/10*) with N-terminal 6 × His and SNAP tags (Breitsprecher *et al.*, 2012).

An isogenic set of *S. cerevisiae* WT and mutant strains was assembled in the S288C background. This included four previously described strains: WT (DDY904: *MATα*, *ura3-52*, *his3Δ200*, *leu203,112*, *trp1-1(am)*; Kozminski *et al.*, 2000), *cof1-22* (Lappalainen *et al.*, 1997), *tpm1Δ* (Alioto *et al.*, 2016), and *pfy1Δ* (Wolven *et al.*, 2000), and three new strains (*cap2Δ*, *aip1Δ*, and *crn1Δ*; BGY3832, BGY3691, and BGY3693) that we generated by homologous recombination in DDY904 and confirmed by genomic DNA PCR analysis.

Protein purification

All protein purification steps were performed on ice or at 4°C unless otherwise noted. The purity of all proteins was assessed by SDS-PAGE and staining with Coomassie Brilliant Blue. Concentrations were calculated by Bradford assay, gel densitometry, and absorbance at 280 nm.

S. cerevisiae actin was purified from commercial baker's yeast (Red Star Yeast, Milwaukee, WI) using DNase I affinity and Mono Q (GE Healthcare, Chicago, IL) chromatography as described (Goode, 2002). Briefly, wet yeast bricks (packed cells) were washed with water and flash frozen in pellets in liquid nitrogen and then mechanically pulverized into a fine powder while submerged in liquid nitrogen using a Waring blender. Powders were stored at –80°C until use. To initiate a preparation, yeast powder was mixed 1:1 (weight:volume) with room temperature G-buffer (5 mM Tris-HCl, pH 8, 0.2 mM ATP, 0.1 mM CaCl₂, 0.5 mM dithiothreitol [DTT]) supplemented with 1× protease inhibitors (0.5 μg/ml each of leupeptin, aprotinin, antipain, chymostatin, and pepstatin A, and 1 mM phenylmethylsulfonyl fluoride) and then centrifuged at 215,000 × *g* for 1 h. Supernatants were loaded onto the DNase I column. The DNase I column was washed with 10 column volumes of: G-buffer, G-buffer with 10% formamide, G-buffer with 0.2 M ammonium chloride, and finally G-buffer alone. Actin was eluted from the column using 2 column volumes of G-buffer with 50% formamide and immediately loaded onto a 1-ml Mono Q column. The Mono Q was washed with 5 ml of G-buffer, and then actin was eluted using a 20-ml linear salt gradient (100–300 mM KCl) in G-buffer. Fractions containing purified actin (which eluted at ~250 mM KCl) were dialyzed three times sequentially over a 48 h period, each time against 1 l of G-buffer. Actin was clarified by centrifugation at 373,000 × *g* for 20 min and flash frozen in 20-μl aliquots, which were stored at –80°C. Three separate preparations of yeast actin, each starting with 100–200 g of yeast powder, yielded 0.6–1.6 mg actin, producing final stock concentrations of 49.2, 44.7, and 41.7 μM.

Rabbit muscle actin (RMA) was purified from acetone powder and Cys-374-labeled with Oregon Green (OG) as described (Spudich and Watt, 1971; Kuhn and Pollard, 2005). Actin was partially extracted from skeletal muscle tissue and stored as “acetone powder” at –80°C. Then, acetone powder was resuspended in G-buffer and cleared by centrifugation at 50,000 × *g*. Actin was polymerized overnight at 4°C by addition of 50 mM NaCl and 2 mM MgCl₂. Then, 0.6 M NaCl was added to F-actin to dissociate actin-binding proteins, and the F-actin was pelleted by centrifugation at 361,000 × *g* for 2.5 h. F-actin pellets were resuspended in G-buffer, dounce homogenized, and dialyzed three times against G-buffer as above.

Actin was polymerized and labeled overnight at 4°C using a 12-fold molar excess of OG-iodoacetamide (Thermo Fisher Scientific, Waltham, MA) in labeling buffer (25 mM imidazole, pH 7.5, 100 mM KCl, 0.15 mM NaATP, and 2 mM MgCl₂). Labeled actin was pelleted at 100,000 × *g* for 3 h at 4°C, resuspended, and dounce homogenized in G-buffer, then dialyzed against G-buffer as above. Labeled G-actin was clarified at 264,000 × *g* for 30 min and then gel filtered using a HiPrep S200 (16/60) column equilibrated in G-buffer. Peak fractions containing OG-RMA were dialyzed against G-buffer with 50% glycerol and stored at –20°C (where it remains stable for months). For experiments performed within 1–2 wk, an aliquot of OG-RMA stored at –20°C was dialyzed against fresh G-buffer and clarified by centrifugation at 353,000 × *g* for 30 min. Preparations of OG-RMA were 85%, 90%, and 80% labeled (27, 52, and 38 μM). Actin concentration was determined by absorbance using a ϵ_{290} of 26,600 M⁻¹cm⁻¹. Labeling percentage calculations assumed the dye concentration was proportional to ϵ_{493} of 77,800 M⁻¹cm⁻¹ with a correction factor (*cf*) of 0.16991 (Eq. 1):

$$[\text{Actin}] = \frac{A_{290} - (A_{493} * cf)}{\epsilon_{290}} \quad (1)$$

6xHis-SNAP-Bni1^{1228–1953} (102.7 kDa) was expressed from a plasmid (pBG1919) introduced into the protease-deficient yeast strain BGY502 (*ura3 leu2 trp1-1 prb1-1122 pep4-3 pre1-451*). Cells were grown to late log-phase (OD₆₀₀ = 0.8) in 2 l synthetic complete media (lacking uracil) with 2% raffinose, then expression was induced by shifting cells to the same media with 2% galactose and adding 20 g bacto-peptone (US Biological, Salem, MA) and 10 g yeast extract (US Biological). After overnight induction at 25°C, yeast were harvested by centrifugation at 4°C at 5000 × *g* for 20 min, washed with water, resuspended in 0.2 vol water, and flash frozen as pellets in liquid N₂. Mechanical lysis was performed using a coffee grinder to pulverize yeast into a fine powder while submerged in liquid N₂. The yeast powder was resuspended and thawed in lysis buffer A (300 mM NaCl and 50 mM NaPO₄, pH 8.0), transferred to ice, and supplemented with 1× protease inhibitors and 0.5 mM DTT. Lysates were clarified two times to remove cellular debris by sequential centrifugation steps at 4°C: first at 28,000 × *g* for 15 min and then at 310,000 × *g* for 30 min. The high-speed supernatant (~20 ml) was then incubated with 0.5 ml Ni²⁺-NTA-agarose resin (Qiagen, Valencia, CA), rotating at 4°C for 1 h. The resin was washed with 100 ml of high salt wash buffer (20 mM imidazole, pH 8.0, 20 mM NaPO₄, pH 8.0, 0.5 mM DTT, and 500 mM NaCl) and then 100 ml of low salt wash buffer (same as above, but with 150 mM NaCl). The protein was eluted from the beads with elution buffer (150 mM NaCl, 250 mM imidazole, pH 8.0, 20 mM NaPO₄, pH 8.0, and 1 mM DTT). The buffer was exchanged to SNAP-labeling buffer (150 mM NaCl, 20 mM NaPO₄, pH 8.0, and 1 mM DTT) using a PD-10 desalting column (GE Healthcare), and the protein was concentrated by Amicon-Ultra filtration (EMD Millipore). The 6xHis-SNAP-Bni1 protein was then mixed with a 2–3 M excess of biotin-Alexa⁵⁴⁹-benzylguanine (New England Biolabs, Ipswich, MA) for 18 h at 4°C, rotating in the dark. To remove excess dye, buffer was exchanged to storage buffer (20 mM HEPES, pH 7.5, 300 mM NaCl, 50% glycerol, and 2 mM DTT) using a 0.5 ml Zeba spin desalting column (Thermo Fisher), and the protein was stored (unfrozen) at –20°C. From 15 g of yeast powder, yields of SNAP-Bni1^{1228–1953} were typically 100 μg, and labeling was 95–100%. Some experiments in this study were performed using SNAP-Bni1^{1228–1953} that was prepared as above but flash frozen in HEKG_{10D} buffer (20 mM HEPES, pH 7.5, 1 mM

EDTA, 10% glycerol, and 2 mM DTT). These two SNAP-Bni1^{1228–1953} preparations had indistinguishable actin cable assembly activities, as determined in TIRF assays. Protein concentration and labeling efficiency was determined by Bradford (using a bovine serum albumin [BSA] standard) and by extinction using $\epsilon_{280} = 66,810 \text{ M}^{-1}\text{cm}^{-1}$ for protein and $\epsilon_{560} = 150,000 \text{ M}^{-1}\text{cm}^{-1}$ for Alexa⁵⁴⁹ with a *cf* of 0.08 (Eq. 1).

Aip1 was purified as described (Rodal *et al.*, 1999, 2002). Glutathione *S*-transferase (GST)-Aip1 was expressed by galactose induction using plasmid pAR3 (pEG(KT)-GST-Aip1) transformed into BGY502 yeast. Cell lysates were prepared as above (see Bni1 purification) with phosphate-buffered saline (PBS) lysis buffer (20 mM NaPO₄, pH 8, 150 mM NaCl, and 1 mM DTT) supplemented with 1× protease inhibitors. Clarified lysates were loaded onto a 5-ml HiTrap Q HP (GE Healthcare) and washed. GST-Aip1 was eluted with a 75-ml linear salt gradient (100–500 mM NaCl) in HD buffer (20 mM HEPES, pH 7.5, 1 mM DTT). Peak fractions (~200 mM NaCl) were pooled and mixed with 1 ml glutathione agarose (Gold Biotechnology, St. Louis, MO) for 1 h at 4°C. The resin was washed with 60 column volumes of PBS and then incubated with 100 U/ml thrombin in PBS for 6 h at room temperature to cleave the GST tag. The eluate (containing released Aip1) was loaded on a 5-ml HiTrapQ HP column, Aip1 was eluted using a salt gradient as above and then concentrated to 30 μM, dialyzed into storage buffer (20 mM HEPES, pH 7.5, 200 mM NaCl, and 1 mM DTT), flash frozen in aliquots, and stored at –80°C.

Cap1/2 was purified as described (Amatruda and Cooper, 1992; Moseley *et al.*, 2004). Untagged Cap1/2 was expressed in yeast by galactose induction as above using the plasmid pBG477 (pGAL1/10-Cap1-Cap2::LEU2). Yeast lysate was prepared in HD buffer and loaded onto a 5-ml HiTrapQ HP column. The column was washed, and Cap1/2 was eluted using a 75-ml linear salt gradient (100–400 mM KCl) in HD buffer. Peak Cap1/2 fractions (~240 mM KCl) were pooled and concentrated, then loaded onto a 120 ml Superdex 75 (16/600) column (GE Healthcare) equilibrated in HKD buffer (20 mM HEPES-KOH pH 7.5, 50 mM KCl, and 1 mM DTT). Cap1/2 eluted just after the void volume (~50 ml), consistent with a 63-kDa complex (Cap1, 30.7 kDa; Cap2, 32.6 kDa). Cap1/2 was further purified on a 1-ml Mono Q column and eluted using a linear salt gradient (100–350 mM KCl) in HD buffer. Cap1/2 was concentrated to 2.8 μM, dialyzed, and stored in HKD buffer, flash frozen in aliquots, and stored at –80°C.

Cof1, Cy3-Cof1^{T46C}, and Crn1 were each purified as previously described (Gandhi *et al.*, 2009; Chaudhry *et al.*, 2013; Mikati *et al.*, 2015). Briefly, each was expressed as a GST-fusion protein in Rosetta 2 (DE3) *Escherichia coli* from pGAT2 plasmids. Cultures were grown at 37°C to 0.8 OD₆₀₀ in Luria broth, and expression was induced with the addition of 0.4 mM isopropyl β-D-1-thiogalactopyranoside (IPTG). After 3 h induction at 37°C, cells were harvested and stored as pellets at –80°C. Cell pellets were resuspended in PBS lysis buffer with 1× protease inhibitors and lysed by sonication on ice. Lysates were clarified by centrifugation at 313,000 × *g* for 30 min at 4°C and then mixed with glutathione agarose for 1 h, rotating at 4°C. The resin was washed with 10 column volumes of PBS and then treated with 0.05 mg/ml thrombin overnight at 4°C in PBS. Released proteins were concentrated and then purified further on a Superdex-75 gel filtration column equilibrated in TN buffer (10 mM Tris-HCl, pH 7.5, 50 mM NaCl, and 1 mM DTT). For labeling, Cof1^{T46C} was dialyzed into degassed TN buffer supplemented with 0.5 mM tris-(2-carboxyethyl)-phosphine HCl instead of DTT and then mixed with a 10-fold molar excess of Cy3-maleimide (GE Healthcare) overnight protected from light at 4°C, rotating. Free dye was removed

using a PD-10 desalting column. All final proteins were in TN buffer and were aliquoted, flash frozen, and stored at –80°C.

Pfy1 was purified as described previously (Wolven *et al.*, 2000; Moseley *et al.*, 2004). Briefly, BL21 (DE3) *E. coli* harboring the pET-derived plasmid pMW172-PFY1 (Eads *et al.*, 1998) were induced as above. Harvested cells were lysed by sonication in 20 mM Tris-HCl, pH 8.0, with 1× protease inhibitors. Lysate was clarified by centrifugation at 310,000 × *g* for 30 min, and Pfy1 and loaded on a 5-ml HiTrap Q column. Pfy1 was eluted using a 75-ml linear salt gradient (0–400 mM NaCl) in 20 mM Tris-HCl, pH 8.0. Peak fractions were pooled, concentrated, and purified further on a Superdex-75 gel filtration column equilibrated in 20 mM Tris-HCl and 50 mM NaCl. Peak fractions of Pfy1 were pooled, aliquoted, flash frozen, and stored at –80°C.

Met-Ala-Ser-(acetyl mimic)-Tpm1 was purified as described (Maytum *et al.*, 2000; Alioto *et al.*, 2016). Briefly, pET DUET-am-Tpm1 (pBG1927) was transformed into BL21 (DE3) *E. coli* and induced with 0.4 mM IPTG as above. Cells were harvested and lysed by sonication in 20 mM Tris-HCl, pH 7.5, 100 mM NaCl, 2 mM EDTA. Next, the lysate was boiled in a 100°C water bath for 10 min and then clarified by centrifugation at 29,000 × *g* for 20 min at room temperature. Tpm1 was precipitated by lowering the pH to its isoelectric point of 4.5 and pelleting at 29,000 × *g* for 20 min. The pellet was dissolved in running buffer (10 mM NaPO₄, pH 7.0, 100 mM NaCl) and purified further (to remove DNA contaminants) on a HiTrap Q HP column, and eluted using a linear salt gradient (100–400 mM NaCl) in running buffer. Peak fractions were pooled and dialyzed into HEK buffer (20 mM HEPES-KOH, pH 7.5, 1 mM EDTA, and 50 mM KCl), aliquoted, flash frozen, and stored at –80°C.

TIRF assays and analysis

For TIRF assays, coverslips were cleaned by 30 min of sonication in detergent, followed by 1 M KOH, 1 M HCl, and stored in 100% ethanol. For passivation and biotinylation, coverslips were washed with water, blown dry with compressed N₂ gas, and coated with a mixture of 4 mg/ml polyethylene glycol (PEG)-silane and 80 μg/ml biotin-PEG in 80% ethanol, pH 1. Coverslips were incubated for 1–3 d at 70°C prior to use. Flow chambers were constructed sandwiching coverslips on plastic flow chambers (Ibidi, Fitchburg, WI) using double-sided tape and epoxy (Devcon, Glenview, IL).

To functionalize beads with formin, 500 ng of biotin-Alexa⁵⁴⁹-Bni1^{1228–1953} were incubated on ice for 30 min with 5 μl of a suspension containing preequilibrated 2-μm diameter biotinylated polystyrene microspheres (Polysciences, Warrington, PA) and 60 μg streptavidin in bead buffer (10 mM imidazole, pH 7.5, 50 mM KCl, 1 mM MgCl₂, 1 mM ethylene-bis(oxyethylenenitrilo)tetraacetic acid [EGTA], and 1 mM DTT). Beads were washed three times with 1 ml of bead buffer and resuspended in 50 μl bead buffer.

For in vitro cable reconstitution experiments, Bni1-coated beads were diluted 10-fold into 1% BSA in HEK buffer and flowed into TIRF chambers, where they were incubated for 5–10 min to allow attachment to the coverslip. Next, the chamber was washed with TIRF buffer (10 mM imidazole, pH 7.5, 75 mM KCl, 1.5 mM MgCl₂, 1.5 mM EGTA, 0.2 mM ATP, 10 mM DTT, 3% dextran, 15 mM glucose, 20 μg/ml catalase, and 100 μg/ml glucose oxidase). Then, reaction mixtures (containing actin, profilin, and other proteins) were rapidly flowed in, and image acquisition was started immediately. Yeast actin was mixed with OG-labeled-RMA to achieve overall 15% labeling of actin, typically yielding a mixture consisting of 0.83 μM yeast actin and 0.17 μM RMA. All other proteins in the reactions were *S. cerevisiae* proteins. Reactions contained one or more of the following proteins, with precise concentrations indicated in the figure legends: 1 μM actin (15% labeled), 1 μM profilin (Pfy1),

30–40 nM capping protein (Cap1/2), 2 μ M tropomyosin (Tpm1; 1 μ M dimers), 200–300 nM cofilin (Cof1), 20 nM coronin (Crn1), and 20 nM Aip1. All protein concentrations were held constant for experiments performed in parallel during each trial used for direct comparison. In some experiments, 300 nM Cy3-Cof1^{T46C} (15% labeled) was used to visualize Cof1 decoration of cables. TIRF assays were performed at room temperature (24–27°C).

To test polarized growth and turnover of cables (Figure 1, H and I), cables were allowed to come to steady state for 1 h using the Complete reaction mixture (which includes labeled actin) and then rapidly washed three times with TIRF buffer and replaced with an identical protein mixture that instead contained unlabeled actin. Over time, unlabeled actin was incorporated into the cable networks and steadily replaced the labeled actin, which revealed the polarity of actin assembly and disassembly.

TIRF microscopy was performed using an inverted Ti200 TIRF microscope system (Nikon Instruments) equipped with 100-mW solid-state lasers (Agilent Technologies), a CFI Apo 60 \times TIRF objective (NA 1.49; Nikon Instruments), and an iXon EMCCD camera (Andor Technology). The Nikon Perfect Focus System was employed to maintain focus. Images were captured every 10–600 s for 10–120 min, depending on the specific experiment. Analysis of images was performed in Fiji ImageJ (Schindelin *et al.*, 2012). Elongation rates and filament lengths were measured using the segmented line tool. Converting changes in actin cable length from μ m s⁻¹ to actin subunits s⁻¹ assumed 370 subunits μ m⁻¹ (Pollard *et al.*, 2000). Fluorescence intensities were measured as mean gray values within 10- μ m circles centered on the beads. Using small circles relative to the average length of cables reduced the contribution of free/background filaments to the fluorescence measurements. Data were normalized to the corresponding “Complete” condition from the same experiment, imaging settings, and point in time. For fluorescence decay analysis in experiments where unlabeled actin was flowed-in experiments (Figure 1, H and I), cable intensities were corrected for the average intensity of the background. Normalized intensity (Figure 2B) was calculated by dividing the intensity samples by the mean intensity around beads in the “Complete” reactions (containing all eight proteins), which were imaged during the same trial using identical settings.

Fixed cell imaging and analysis

For comparing actin cable organization in WT and mutant yeast strains, we used SIM and confocal microscopy. SIM was used to gain a more detailed view of cable networks, because of its improved resolution over conventional light microscopy. Yeast cells were grown at 25°C in YEPD-rich media to mid-log phase (OD₆₀₀ 0.4–0.6), then fixed in 4.7% formaldehyde for 45 min, and washed three times in PBS. To remove actin patches, cells were pretreated with 100 μ M CK666 for 15 min at 25°C before fixation. Cells were stained overnight with Alexa⁴⁸⁸-phalloidin (Life Technologies) and then washed twice with PBS and mounted on glass slides. For SIM, cells were imaged on a Ti-2 SIM-E inverted microscope with a 100 \times oil objective (NA 1.49) and Hamamatsu Orca Flash 4.0 camera controlled by NIS-Elements software (Nikon Instruments) at ambient temperature. Z-series of SIM reconstructions were flattened to a single image by maximum projection (Figures 1A and 3A). SIM was used to quantify cable levels in untreated cells because it allows more accurate tracing of individual cables. In sum intensity projection images, we traced the cables in the mother compartment to obtain total cable length and total fluorescence signal in cables for each cell. These values were used to calculate mean total cable fluorescence (in the mother compartment), which we normalized as a percentage of WT. Confocal microscopy was used to measure cable

density in CK666-treated cells, instead of SIM, because 1) it allowed us to obtain and analyze larger datasets, and 2) it was more reliable and reproducible in measuring cable fluorescence intensity (since SIM produces reconstructed images extracted from raw data). For confocal imaging, cell images were captured on an i-E upright microscope equipped with a CSU-W1 spinning disk head, 100 \times oil objective (NA 1.4) and an Ixon 897 Ultra-CCD camera controlled by NIS-Elements software (Nikon Instruments). Actin cable density (fluorescence per unit area) was determined for cells treated with CK666 by measuring the total fluorescence in the cell or mother compartment (as indicated in the figure legends) from the sum intensity projection, subtracting the intensity of an adjacent background region, and dividing by the area of the cell.

Graphing and statistical analyses

Graphing and statistical analyses were performed using GraphPad Prism 8.2.1. Comparisons of fluorescence intensity data were made using nonparametric one-way analysis of variance (ANOVA) (Kruskal–Wallis test). Mann–Whitney nonparametric *t* tests were used to compare *in vitro* cable lengths. In figures, *P* value is indicated by ns for *P* > 0.05, * for *P* ≤ 0.05, ** for *P* ≤ 0.01, *** for *P* ≤ 0.001, and **** for *P* ≤ 0.0001.

ACKNOWLEDGMENTS

We thank Steven DelSignore, Colby Fees, Greg Hoeprich, M. Angeles Juanes, Qing Tang, and Alison Wirshing for helpful comments on the manuscript. We thank Chenyu Lou for helping with early experiments contributing to Figure 2, B and C. This work was funded by National Institute of General Medical Sciences/National Institutes of Health grants F32 GM131541 to L.W.P. and R01 GM083137 and R01 GM063691 to B.L.G.

REFERENCES

- Adams AE, Cooper JA, Drubin DG (1993). Unexpected combinations of null mutations in genes encoding the actin cytoskeleton are lethal in yeast. *Mol Biol Cell* 4, 459–468.
- Alioto SL, Garabedian MV, Bellavance DR, Goode BL (2016). Tropomyosin and profilin cooperate to promote formin-mediated actin nucleation and drive yeast actin cable assembly. *Curr Biol* 26, 3230–3237.
- Amatruda JF, Cannon JF, Tatchell K, Hug C, Cooper JA (1990). Disruption of the actin cytoskeleton in yeast capping protein mutants. *Nature* 344, 352–354.
- Amatruda JF, Cooper JA (1992). Purification, characterization, and immunofluorescence localization of *Saccharomyces cerevisiae* capping protein. *J Cell Biol* 117, 1067–1076.
- Antkowiak A, Guillotin A, Boiero Sanders M, Colombo J, Vincentelli R, Michelot A (2019). Sizes of actin networks sharing a common environment are determined by the relative rates of assembly. *PLoS Biol* 17, e3000317.
- Asakura T, Sasaki T, Nagano F, Satoh A, Obaishi H, Nishioka H, Imamura H, Hotta K, Tanaka K, Nakanishi H, *et al.* (1998). Isolation and characterization of a novel actin filament-binding protein from *Saccharomyces cerevisiae*. *Oncogene* 16, 121–130.
- Breitsprecher D, Jaiswal R, Bombardier JP, Gould CJ, Gelles J, Goode BL (2012). Rocket launcher mechanism of collaborative actin assembly defined by single-molecule imaging. *Science* 336, 1164–1168.
- Brieher WM, Kueh HY, Ballif BA, Mitchison TJ (2006). Rapid actin monomer-insensitive depolymerization of *Listeria* actin comet tails by cofilin, coronin, and Aip1. *J Cell Biol* 175, 315–324.
- Burke TA, Christensen JR, Barone E, Suarez C, Sirotkin V, Kovar DR (2014). Homeostatic actin cytoskeleton networks are regulated by assembly factor competition for monomers. *Curr Biol* 24, 579–585.
- Buttery SM, Kono K, Stokasimov E, Pellman D (2012). Regulation of the formin Bnr1 by septins and MARK/Par1-family septin-associated kinase. *Mol Biol Cell* 23, 4041–4053.
- Buttery SM, Yoshida S, Pellman D (2007). Yeast formins Bni1 and Bnr1 utilize different modes of cortical interaction during the assembly of actin cables. *Mol Biol Cell* 18, 1826–1838.

- Chaudhry F, Breitsprecher D, Little K, Sharov G, Sokolova O, Goode BL (2013). Srv2/cyclase-associated protein forms hexameric shurikens that directly catalyze actin filament severing by cofilin. *Mol Biol Cell* 24, 31–41.
- Christensen JR, Hocky GM, Homa KE, Morganthaler AN, Hitchcock-DeGregori SE, Voth GA, Kovar DR (2017). Competition between Tropomyosin, Fimbrin, and ADF/Cofilin drives their sorting to distinct actin filament networks. *eLife* 6, e23152.
- Christensen JR, Homa KE, Morganthaler AN, Brown RR, Suarez C, Harker AJ, O'Connell ME, Kovar DR (2019). Cooperation between tropomyosin and alpha-actinin inhibits fimbrin association with actin filament networks in fission yeast. *eLife* 8, e47279.
- Drubin DG, Miller KG, Botstein D (1988). Yeast actin-binding proteins: evidence for a role in morphogenesis. *J Cell Biol* 107, 2551–2561.
- Eads JC, Mahoney NM, Vorobiev S, Bresnick AR, Wen KK, Rubenstein PA, Haarer BK, Almo SC (1998). Structure determination and characterization of *Saccharomyces cerevisiae* profilin. *Biochemistry* 37, 11171–11181.
- Eskin JA, Rankova A, Johnston AB, Alioto SL, Goode BL (2016). Common formin-regulating sequences in Smy1 and Bud14 are required for the control of actin cable assembly in vivo. *Mol Biol Cell* 27, 828–837.
- Evangelista M, Pruyn D, Amberg DC, Boone C, Bretscher A (2002). Formins direct Arp2/3-independent actin filament assembly to polarize cell growth in yeast. *Nat Cell Biol* 4, 32–41.
- Gandhi M, Achard V, Blanchoin L, Goode BL (2009). Coronin switches roles in actin disassembly depending on the nucleotide state of actin. *Mol Cell* 34, 364–374.
- Ganzinger KA, Schwille P (2019). More from less—bottom-up reconstitution of cell biology. *J Cell Sci* 132, jcs227488.
- Gao L, Liu W, Bretscher A (2010). The yeast formin Bnr1p has two localization regions that show spatially and temporally distinct association with septin structures. *Mol Biol Cell* 21, 1253–1262.
- Garabedian MV, Stanishneva-Konovalova T, Lou C, Rands TJ, Pollard LW, Sokolova OS, Goode BL (2018). Integrated control of formin-mediated actin assembly by a stationary inhibitor and a mobile activator. *J Cell Biol* 217, 3512–3530.
- Goode BL (2002). Purification of yeast actin and actin-associated proteins. *Methods Enzymol* 351, 433–441.
- Goode BL, Eskin JA, Wendland B (2015). Actin and endocytosis in budding yeast. *Genetics* 199, 315–358.
- Goode BL, Wong JJ, Butty AC, Peter M, McCormack AL, Yates JR, Drubin DG, Barnes G (1999). Coronin promotes the rapid assembly and cross-linking of actin filaments and may link the actin and microtubule cytoskeletons in yeast. *J Cell Biol* 144, 83–98.
- Graziano BR, Yu HY, Alioto SL, Eskin JA, Ydenberg CA, Waterman DP, Garabedian M, Goode BL (2014). The F-BAR protein Hof1 tunes formin activity to sculpt actin cables during polarized growth. *Mol Biol Cell* 25, 1730–1743.
- Haarer BK, Lillie SH, Adams AE, Magdolen V, Bandlow W, Brown SS (1990). Purification of profilin from *Saccharomyces cerevisiae* and analysis of profilin-deficient cells. *J Cell Biol* 110, 105–114.
- Iida K, Moriyama K, Matsumoto S, Kawasaki H, Nishida E, Yahara I (1993). Isolation of a yeast essential gene, COF1, that encodes a homologue of mammalian cofilin, a low-M(r) actin-binding and depolymerizing protein. *Gene* 124, 115–120.
- Jansen S, Collins A, Chin SM, Ydenberg CA, Gelles J, Goode BL (2015). Single-molecule imaging of a three-component ordered actin disassembly mechanism. *Nat Commun* 6, 7202.
- Jansen S, Goode BL (2019). Tropomyosin isoforms differentially tune actin filament length and disassembly. *Mol Biol Cell* 30, 671–679.
- Kamasaki T, Arai R, Osumi M, Mabuchi I (2005). Directionality of F-actin cables changes during the fission yeast cell cycle. *Nat Cell Biol* 7, 916–917.
- Karsenti E (2008). Self-organization in cell biology: a brief history. *Nat Rev Mol Cell Biol* 9, 255–262.
- Kovar DR, Harris ES, Mahaffy R, Higgs HN, Pollard TD (2006). Control of the assembly of ATP- and ADP-actin by formins and profilin. *Cell* 124, 423–435.
- Kozminski KG, Chen AJ, Rodal AA, Drubin DG (2000). Functions and functional domains of the GTPase Cdc42p. *Mol Biol Cell* 11, 339–354.
- Kuhn JR, Pollard TD (2005). Real-time measurements of actin filament polymerization by total internal reflection fluorescence microscopy. *Biophys J* 88, 1387–1402.
- Kukulski W, Schorb M, Kaksonen M, Briggs JA (2012). Plasma membrane reshaping during endocytosis is revealed by time-resolved electron tomography. *Cell* 150, 508–520.
- Lappalainen P, Fedorov EV, Fedorov AA, Almo SC, Drubin DG (1997). Essential functions and actin-binding surfaces of yeast cofilin revealed by systematic mutagenesis. *EMBO J* 16, 5520–5530.
- Levy DL, Heald R (2012). Mechanisms of intracellular scaling. *Annu Rev Cell Dev Biol* 28, 113–135.
- Loisel TP, Boujemaa R, Pantaloni D, Carlier MF (1999). Reconstitution of actin-based motility of *Listeria* and *Shigella* using pure proteins. *Nature* 401, 613–616.
- Marshall WF (2016). Cell geometry: how cells count and measure size. *Annu Rev Biophys* 45, 49–64.
- Martin SG, Chang F (2006). Dynamics of the formin for3p in actin cable assembly. *Curr Biol* 16, 1161–1170.
- Maytum R, Geeves MA, Konrad M (2000). Actomyosin regulatory properties of yeast tropomyosin are dependent upon N-terminal modification. *Biochemistry* 39, 11913–11920.
- Miao Y, Han X, Zheng L, Xie Y, Mu Y, Yates JR 3rd, Drubin DG (2016). Fimbrin phosphorylation by metaphase Cdk1 regulates actin cable dynamics in budding yeast. *Nat Commun* 7, 11265.
- Miao Y, Wong CC, Mennella V, Michelot A, Agard DA, Holt LJ, Yates JR 3rd, Drubin DG (2013). Cell-cycle regulation of formin-mediated actin cable assembly. *Proc Natl Acad Sci USA* 110, E4446–E4455.
- Michelot A, Berro J, Guerin C, Boujemaa-Paterski R, Staiger CJ, Martiel JL, Blanchoin L (2007). Actin-filament stochastic dynamics mediated by ADF/cofilin. *Curr Biol* 17, 825–833.
- Mikati MA, Breitsprecher D, Jansen S, Reisler E, Goode BL (2015). Coronin enhances actin filament severing by recruiting cofilin to filament sides and altering F-actin conformation. *J Mol Biol* 427, 3137–3147.
- Mishra M, Kashiwazaki J, Takagi T, Srinivasan R, Huang Y, Balasubramanian MK, Mabuchi I (2013). In vitro contraction of cytokinetic ring depends on myosin II but not on actin dynamics. *Nat Cell Biol* 15, 853–859.
- Misteli T (2001). The concept of self-organization in cellular architecture. *J Cell Biol* 155, 181–185.
- Moon AL, Janmey PA, Louie KA, Drubin DG (1993). Cofilin is an essential component of the yeast cortical cytoskeleton. *J Cell Biol* 120, 421–435.
- Moseley JB, Goode BL (2006). The yeast actin cytoskeleton: from cellular function to biochemical mechanism. *Microbiol Mol Biol Rev* 70, 605–645.
- Moseley JB, Maiti S, Goode BL (2006). Formin proteins: purification and measurement of effects on actin assembly. *Methods Enzymol* 406, 215–234.
- Moseley JB, Sagot I, Manning AL, Xu Y, Eck MJ, Pellman D, Goode BL (2004). A conserved mechanism for Bni1- and mDia1-induced actin assembly and dual regulation of Bni1 by Bud6 and profilin. *Mol Biol Cell* 15, 896–907.
- Okada K, Ravi H, Smith EM, Goode BL (2006). Aip1 and cofilin promote rapid turnover of yeast actin patches and cables: a coordinated mechanism for severing and capping filaments. *Mol Biol Cell* 17, 2855–2868.
- Pollard TD, Blanchoin L, Mullins RD (2000). Molecular mechanisms controlling actin filament dynamics in nonmuscle cells. *Annu Rev Biophys Biomol Struct* 29, 545–576.
- Pruyn DW, Schott DH, Bretscher A (1998). Tropomyosin-containing actin cables direct the Myo2p-dependent polarized delivery of secretory vesicles in budding yeast. *J Cell Biol* 143, 1931–1945.
- Rodal AA, Duncan M, Drubin D (2002). Purification of glutathione S-transferase fusion proteins from yeast. *Methods Enzymol* 351, 168–172.
- Rodal AA, Tetreault JW, Lappalainen P, Drubin DG, Amberg DC (1999). Aip1p interacts with cofilin to disassemble actin filaments. *J Cell Biol* 145, 1251–1264.
- Romero S, Didry D, Larquet E, Boisset N, Pantaloni D, Carlier MF (2007). How ATP hydrolysis controls filament assembly from profilin-actin: implication for formin processivity. *J Biol Chem* 282, 8435–8445.
- Sagot I, Klee SK, Pellman D (2002). Yeast formins regulate cell polarity by controlling the assembly of actin cables. *Nat Cell Biol* 4, 42–50.
- Schindelin J, Arganda-Carreras I, Frise E, Kaynig V, Longair M, Pietzsch T, Preibisch S, Rueden C, Saalfeld S, Schmid B, et al. (2012). Fiji: an open-source platform for biological-image analysis. *Nat Methods* 9, 676–682.
- Shekhar S, Carlier MF (2017). Enhanced depolymerization of actin filaments by ADF/cofilin and monomer funneling by capping protein cooperate to accelerate barbed-end growth. *Curr Biol* 27, 1990–1998.e1995.
- Skau CT, Kovar DR (2010). Fimbrin and tropomyosin competition regulates endocytosis and cytokinesis kinetics in fission yeast. *Curr Biol* 20, 1415–1422.
- Spudich JA, Watt S (1971). The regulation of rabbit skeletal muscle contraction. I. Biochemical studies of the interaction of the

- tropomyosin-troponin complex with actin and the proteolytic fragments of myosin. *J Biol Chem* 246, 4866–4871.
- Suarez C, Carroll RT, Burke TA, Christensen JR, Bestul AJ, Sees JA, James ML, Sirotkin V, Kovar DR (2015). Profilin regulates F-actin network homeostasis by favoring formin over Arp2/3 complex. *Dev Cell* 32, 43–53.
- Suarez C, Kovar DR (2016). Internetwork competition for monomers governs actin cytoskeleton organization. *Nat Rev Mol Cell Biol* 17, 799–810.
- Wedlich-Soldner R, Betz T (2018). Self-organization: the fundament of cell biology. *Philos Trans R Soc Lond B Biol Sci* 373, 20170103.
- Wolven AK, Belmont LD, Mahoney NM, Almo SC, Drubin DG (2000). In vivo importance of actin nucleotide exchange catalyzed by profilin. *J Cell Biol* 150, 895–904.
- Yang HC, Pon LA (2002). Actin cable dynamics in budding yeast. *Proc Natl Acad Sci USA* 99, 751–756.
- Ydenberg CA, Johnston A, Weinstein J, Bellavance D, Jansen S, Goode BL (2015). Combinatorial genetic analysis of a network of actin disassembly-promoting factors. *Cytoskeleton* 72, 349–361.
- Yu JH, Crevenna AH, Bettenbuhl M, Freisinger T, Wedlich-Soldner R (2011). Cortical actin dynamics driven by formins and myosin V. *J Cell Sci* 124, 1533–1541.